Novel Corner-Reflector Array Application in Essential Infrastructure Monitoring

Krisztina Kelevitz [ID], Tim J Wright [ID], Andrew J Hooper [ID], *Senior Member, IEEE*,
and Sivasakthy Selvakumaran [ID], *Member, IEEE*

Abstract—**High-precision monitoring of infrastructure using artificial reflectors is possible with freely available Sentinel-1 data, but large reflectors are needed. We find that a triangular trihedral corner reflector should typically have at least 1-m inner leg length. As such large reflectors are often not feasible for use in urban areas for essential infrastructure monitoring, we designed a multiple corner-reflector array to replace a single corner reflector with an inner leg length of 1 m. In this case, we use four reflectors where each of them is a truncated triangular trihedral with an inner leg length of 0.33 m. We measured interferometric synthetic aperture radar (InSAR) amplitude, phase, and coherence of this reflector array with various configurations of alignments of the array. We find that as long as great care is taken in the relative positioning of the four corner reflectors, so that they constructively interfere, each horizontal or vertical configuration provides the expected amplitude, coherence, and phase stability. Applications of multiple small corner reflectors in urban areas range from essential infrastructure monitoring (e.g., bridges, overpasses, and tunnel constructions), through assessment of structural health of buildings, to monitoring highway and railway embankments. We show that the multiple corner array works when placed in a single InSAR resolution cell, but depending on the application, the number and projection of corner reflectors can be varied, as long as sufficient signal-to-clutter ratio is achieved in the area of interest.**

Index Terms—**Corner reflectors, infrastructure monitoring, interferometric synthetic aperture radar (InSAR).**

I. INTRODUCTION

OUR ever-expanding structural infrastructure is in constant need of monitoring and maintenance due to damage from regular use and exposure to natural processes. It is near-impossible to manually inspect all the bridges, railways, highways, and other essential infrastructure to predict and avoid failures that might result in loss of life and great economic losses. Recent advances in various remote sensing methods have improved our capabilities to monitor large areas with various techniques of different temporal and spatial resolutions.

In particular, interferometric synthetic aperture radar (InSAR) is being widely used for ground motion detection for various applications ranging from worldwide natural hazard monitoring (e.g., [1]) and early warning (e.g., [2], [3]) through nationwide infrastructure and land observation (e.g., [4], [5]) to small-scale studies of local deformations (e.g., [6], [7]). The Sentinel-1 mission, part of the European Commision's Copernicus program operated by the European Space Agency (ESA), was launched in 2014 and has been providing freely available SAR acquisitions globally ever since (https://www.copernicus.eu/en, accessed on 4 Jun 2021). The Sentinel 1A and 1B satellite pair provides an ascending and a descending coverage at least once every six days over Europe. This mission has furthered applications of InSAR remote sensing due to its reliability, repeatability, and all-reaching coverage. Sentinel-1 is a C-band mission ($\sim$6 cm wavelength) which provides moderate resolution InSAR data compared with the commercial, high-resolution X-band satellite missions (e.g., TerraSAR-X, COSMO-SkyMed). The C-band missions are typically used for global mapping and monitoring and detecting changes in areas with low to moderate penetration. The X-band missions, on the other hand, are traditionally used for urban monitoring and in areas with low vegetation levels.

At the C-band, Sentinel-1 InSAR acquisitions are often not coherent enough over rural, vegetated areas to interpret ground motions in these places. To enhance the InSAR amplitudes and measurement accuracy, corner reflectors can be used in these settings. Among the applications of corner reflectors are landslide monitoring [8], [9], land management [10], ground instability observations [11], or calibration of InSAR and other geophysical observations [12]. Based on a literature and corner reflector database review, the size of these corner reflectors can range from a 0.35-m up to 3-m inner leg length depending on the area of interest and the InSAR mission that it is targeted toward. [Red line of Fig. 8(b) shows the measurement of the inner leg length on a triangular trihedral corner reflector.] To use a corner reflector with the Sentinel-1 InSAR mission, the reflector needs to be quite large; Bozsó *et al.* [13] showed that a triangular trihedral of 1-m inner leg length provides a robust signal for Sentinel-1 [13].

Large corner reflectors may not be suitable for urban applications, as there are often limits on the size of objects that can be attached to buildings or infrastructure such as bridges. In particular, the projection of the reflector can

be a limiting factor. In this article, we show the results of an experiment using a novel corner reflector array that has a reduced projection, but retains the ability to reflect a strong enough SAR signal so that it can be used with data from the moderate resolution Sentinel-1 InSAR application. The array consists of four reflectors arranged closely in a row, so that they remain in a single resolution cell of an SAR image. We tested various configurations in terms of aligning the reflectors in different directions horizontally, vertically, and arbitrarily and found that in each configuration we can measure a stable amplitude and phase signal. Our setup consists of four reflectors and a frame on which they can be placed in various configurations to allow for various experiments.

We present the design, manufacturing considerations, and InSAR measurement results as well as the practical considerations that should be taken into account when installing such a reflector array. Based on the theoretical calculations and the results from this experiment, we show that any number of corner reflectors can be placed within a single pixel, with the conclusion that the more the reflectors, the smaller their overall projections, as long as the size is not much smaller than the radar wavelength. This opens a new area of applications of the corner reflectors and the use of the C-band SAR missions, especially into the urban areas for infrastructure monitoring.

In Section II, we review the amplitude and phase theory of corner reflectors and show the results of Sentinel-1 SAR data processing of various corner reflectors around the world. In Section III, we show the design and setup of the four-corner array and the results of InSAR and global navigation satellite systems (GNSS) data processing of various setups. We also discuss the practical considerations that one should take into account when deploying a corner reflector array. In Section IV, we discuss the practical considerations concerning the installation and setup of the four-corner array. In Section V, we present our conclusions.

II. SINGLE CORNER REFLECTORS

A. Review of Amplitude and Phase of a Single Corner Reflector

The measurement of the size of the target as seen by the imaging radar is the radar cross section (RCS) [14]. The brightness of a target or backscattering coefficient "sigma nought" (σ_0) is conventionally measured as the RCS (in dBm^2) normalized by the area of the illuminated resolution cell [15]

$$\sigma_0 = \frac{\text{RCS}}{A} \qquad (1)$$

where the illuminated area on the ground is

$$A = \frac{p_r p_a}{\sin \theta} \qquad (2)$$

where p_a and p_r are the azimuth and slant range pixel resolutions, respectively, and θ is the local incidence angle.

The theoretical RCS, often denoted as σ_T, of a triangular trihedral corner reflector that is significantly larger than the SAR wavelength is a function of its size [16]

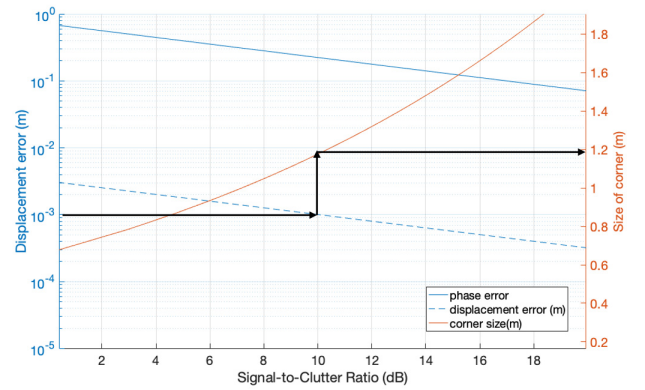$$\sigma_T = \frac{4\pi a^4}{3\lambda^2} \qquad (3)$$

Fig. 1. SCR and the corresponding error in phase (blue solid line) and displacement (blue dashed line). The orange line shows the size of a trihedral corner reflector compared with the SCR it produces, assuming a 15.8-dB background clutter amplitude. The black arrows show the following example: to achieve mm-level precision in the displacement measurement, the SCR needs to be at least 10 dB, which corresponds to a trihedral corner reflector with a 1.2-m-long inner leg with the defined background clutter level.

where a is the inner leg of the trihedral corner reflector, and λ is the wavelength of the acquisition.

The expected amplitude is calculated from the RCS as

$$\text{amp} = \sqrt{\sigma_T}. \qquad (4)$$

The ratio of the RCS of a corner reflector and the power of its background clutter, the signal-to-clutter ratio (SCR), is used to assess the InSAR phase variance [17] and absolute positioning accuracy [18] of point targets, such as corner reflectors [19]. This determines whether a corner reflector's size is sufficient to be used in a certain setting with a particular clutter level.

The phase and displacement errors can be theoretically estimated using the SCR as [20], [21], [22]

$$\varphi_{\text{err}} = \frac{1}{\sqrt{2\text{SCR}}} \qquad (5)$$

$$d_{\text{err}} = \frac{\varphi_{\text{err}} \lambda}{4\pi}. \qquad (6)$$

Fig. 1 shows the displacement precision that can be achieved with a certain size of corner reflector as a function of SCR assuming a 15.8-dB background clutter level. This figure and its calculations are based on the Sentinel-1 wavelength of 5.55 cm and is representative of the C-band SAR acquisitions; the figure would look different for the X-band or L-band.

When designing an experiment with a corner reflector, it is useful to know about the clutter level in the area of installation ahead of planning. To have a large enough reflector to be "visible" in the desired setting, one should achieve a certain level of SCR, which will then give phase and displacement precisions for the intended application.

B. Corner Reflectors Installed Globally

We collected information about corner reflectors that have been placed in various locations around the world and categorized them in terms of their shape, size, and orientation. Most are triangular trihedrals or truncated triangular trihedrals,

with the exception of the bar-pattern reflector in China. The size of the triangular trihedrals varies between an inner leg length of 0.35 and 3 m. When discussing the size of a truncated triangular trihedral corner reflector, we use the inner leg length without truncation, as that is representative of its reflecting abilities. We processed the Sentinel-1 SAR data over their locations. The SAR data were acquired in the Interferometric Wide swath mode using Terrain Observation with Progressive Scans (IW TOPSAR) mode with a nominal resolution of approximately 5 m by 20 m. Some reflectors were installed before the launch of the Sentinel-1 satellites; in these cases, we processed the earliest available data. Others were installed after 2015; in these cases, we aimed to process the SAR data before and after the installation of the corner reflectors and compared the change in amplitude and phase at their locations. Table I shows the locations, sizes, shape specifications, and references to these corner reflectors. For this section, we relied on other studies that provided us the lat/lon coordinates of the reflectors, and we assume they used GNSS instruments to get the precise position of each reflector. References to each of the study areas are shown in Table I. We obtained the coordinates either from these publications, through personal communication with the authors, or from the "Point & Distributed Targets DB" database (https://calvalportal.ceos.org/point-distributed-targets-db;jsessionid=574D708265484DA9A87C50BA6E548FF0).

We used the GAMMA-based [29] LiCSAR [30] batch processing software package, at full resolution, for assessing amplitudes and phases of individual pixels. After coregistering single-look complex (SLC) images, we extracted the amplitude at, and around, the location of the corner reflectors and compared them before (where possible) and after the installation of the corner reflectors. We then formed interferograms with a common primary image, selecting the primary to be the first available image after the installation of the corner reflectors.

C. Sentinel-1 InSAR Results

Fig. 2 shows photographs of the selected corner reflectors. We analyzed their amplitude and phase signal on coregistered SLC images. We used Gamma's geocoding procedure to find the location of the corner reflectors in the radar coordinates and then confirmed these locations against known features nearby.

The amplitude images are shown with the location of the reflectors marked (Figs. 3–5). These figures show the average amplitude values that are obtained by calculating the mean amplitude values over multiple acquisitions from the coregistered stacks. For a complete collection of the amplitude figures, refer to the Appendix.

From the interferograms, we extract the phase information of various pixels: 1) the pixel corresponding to the corner reflector; 2) a "stable" pixel nearby, typically corresponding to a building; and 3) a "noisy" pixel nearby, typically corresponding to the vegetated area. These pixels were selected manually based on their consistently high (stable) or varying (noisy) amplitudes. To assess the phase stability of the corner reflector, we plot the differences between the phase signals of
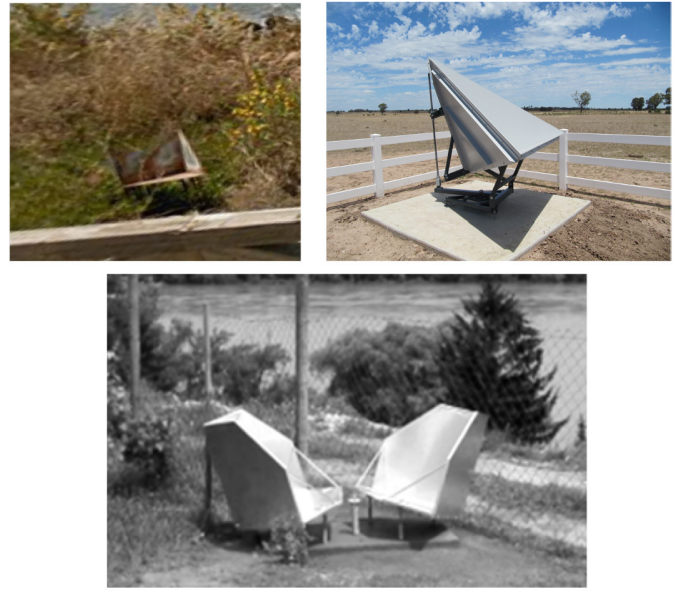

Fig. 2. (Top Left) Photograph of a reflector at Capo Colonna; source: Google Street View. (Top Right) Photograph of a 1.5-m reflector in Australia; source: Garthwaite *et al.* [12]. (Bottom) Photograph of the twin reflectors in Kulcs, Hungary; source: Bozsó *et al.* [25].
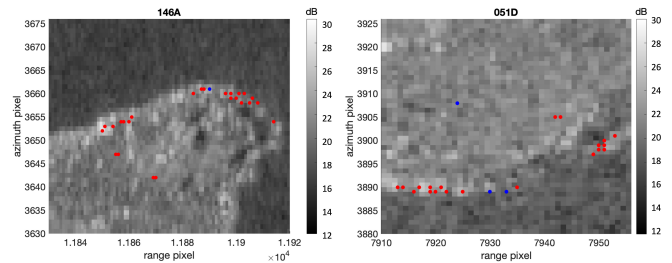

Fig. 3. Average amplitudes of corner reflectors at the archeological site of Capo Colonna. (Left) 146A ascending track. (Right) 051D descending track. These reflectors are too small to stand out from the background with Sentinel-1 with a trihedral inner leg measure of 0.4 m. Red dots mark pixels with one reflector, and blue dots mark pixels with two reflectors placed there.

1) the "stable" and "noisy" pixels and of and 2) the "stable" and corner reflector pixels (Fig. 6. For a complete collection of the phase figures, refer to the Appendix. We expect the latter differential phase signal to be less noisy (i.e., smaller standard deviation from the mean of the series) than that of the former. In cases where corner reflectors were installed after the launch of Sentinel-1, and their size is sufficiently large to be visibly differentiable from the background on the amplitude analysis, we can also observe the stabilization of the phase after the reflector was installed (Fig. 6).

We find that a trihedral corner reflector with an inner leg of at least 1 m is sufficiently large to give a stable phase response, and one with an inner leg of up to 0.6 m appears to be too small for the C-band Sentinel-1 acquisitions. We cannot conclude a clear cut-off in size, as we do not have any InSAR data processed for a corner reflector that is between 0.6 and 1 m. One example where smaller reflectors (0.35-m inner leg triangular trihedrals) were installed after the launch of the Sentinel-1 mission is a study on the Waterloo Bridge in

TABLE I

LIST OF CORNER REFLECTORS. IN THE CASE OF TRUNCATED TRIHEDRAL CORNER REFLECTORS, THE SIZE IS GIVEN AS THE INNER LEG OF THE TRIHEDRAL WITHOUT THE TRUNCATION TO MAKE FAIR COMPARISONS. THE FIGURE COLUMN SHOWS WHICH FIGURES CORRESPOND TO WHICH LOCATION IN THIS ARTICLE

| Location	Size	Shape	Installation date	Reference	Figure
Waterloo Bridge (UK)	0.35 m	trihedral	December 2017	[23]	Figure 7
Capo Colonna (Italy)	0.4 m	trihedral	July 2015	[11]	Figure 3
Pisciotta 1 (Italy)	0.6 m	trihedral	Nov 2016	[10]	Figures 16 & 17
Pisciotta 2 (Italy)	0.6 m	trihedral	Nov 2016	[10]	Figures 18 & 19
Calitri (Italy)	1 m	truncated trihedral	2008	[24]	Figure 28
Dunaszekcsö (Hungary)	1 m	truncated trihedral	February 2017	[13]	Figure 25
Kulcs (Hungary)	1 m	truncated trihedral	September 2016	[25]	Figures 4 & 6
Fonyód (Hungary)	1 m	truncated trihedral	October 2016	[13]	Figures 26 & 27
Herstmonceux (UK)	1 m	truncated trihedral	March 2020		Figures 22 & 23 & 24
Hollin Hill (UK)	1 m	truncated trihedral	July 2019		Figures 20 & 21
Baotou (China)	various	bar pattern	2014	[26]	Figure 20
Agnone (Italy)	1.4 m	truncated trihedral	2009	[27]	Figure 29
Surat basin (Australia)	1.5 m	trihedral	November 2014	[12], [28]	Figure 5
Surat basin (Australia)	2 m	trihedral	November 2014	[12], [28]	Figure 5
Surat basin (Australia)	2.5 m	trihedral	November 2014	[12], [28]	Figure 5
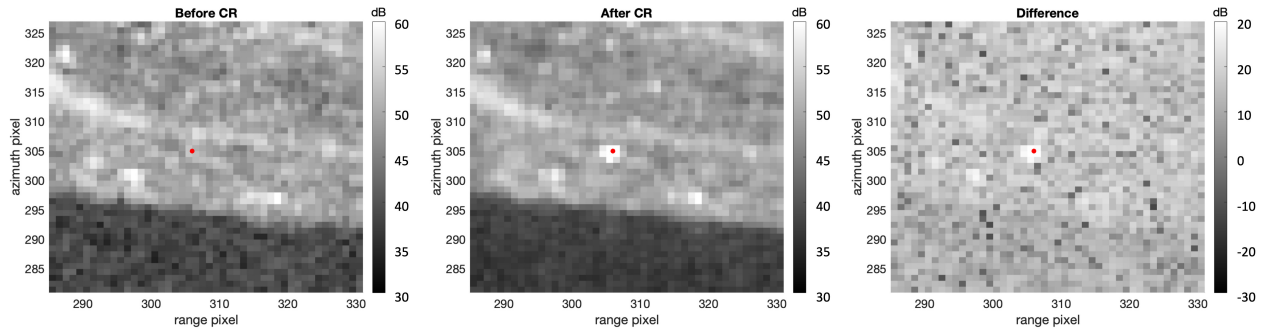
Fig. 4. Amplitudes of one of the four corner reflectors installed near the town of Kulcs in Hungary recorded with the 051D descending track of Sentinel-1. (Left) Before placement of the reflector. (Middle) After placement of the reflector. (Right) Difference.
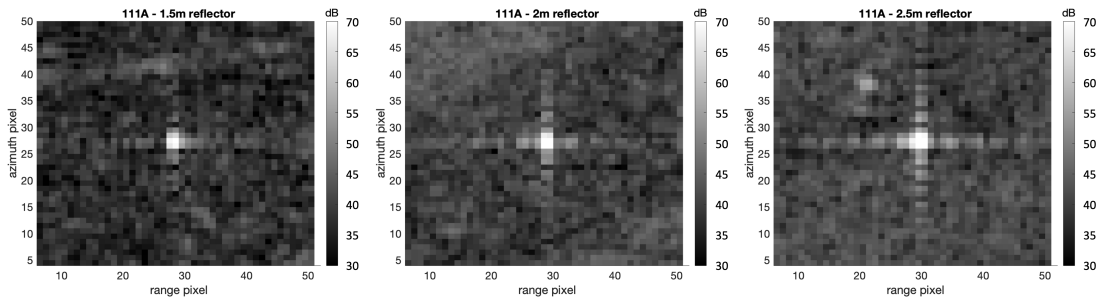

Fig. 5. Amplitudes of corner reflectors of different sizes installed in the Surat basin in Australia recorded with the 111A ascending track of Sentinel-1. (Left) 1.5-m inner leg trihedral. (Middle) 2-m inner leg trihedral. (Right) 2.5-m inner leg trihedral.

London [23]. These corner reflectors were originally designed to be used with the X-band SAR missions, rather than the C-band Sentinel-1 one, and are therefore not optimally oriented. We compared the amplitude and phase signal before and after the installation and we find that even though the smaller reflectors do not appear on the amplitude maps, it seems they still contribute to a small stabilization of the phase signal (Fig. 7). Analysis of coherence of the example corner reflectors presented here and the corner reflectors listed in Table I is shown in the Appendix Fig. 32.

III. MULTIREFLECTOR EXPERIMENT

A. Design and Setup

In Section II-A, we show the calculations for the precision that can be achieved with a certain size of corner reflector as a function of SCR. Assuming the signals' sum constructively, we can calculate how many small reflectors one would need to place in the same pixel to replace a large reflector with an inner leg length of 1 m [Fig. 8(a)]. Based on this distribution, and the analysis in Section II-C which showed that a 1-m corner reflector is sufficiently large to be seen with the Sentinel-1 data, we manufactured a frame with four small trihedral corner reflectors with a 0.- m inner leg [Fig. 8(b)]. With the truncated design that we chose [Fig. 8(b) and also seen in the middle panel of Fig. 2], the actual inner leg length of each reflector is 0.33 m. Based on the calculations shown in Fig. 1, this should give close to mm-level precision in displacement. Fig. 8(c) shows the calculations of the expected amplitudes in decibel (dB) depending on the size and number of triangular trihedral corner reflectors placed in the same pixel. Again, we stress
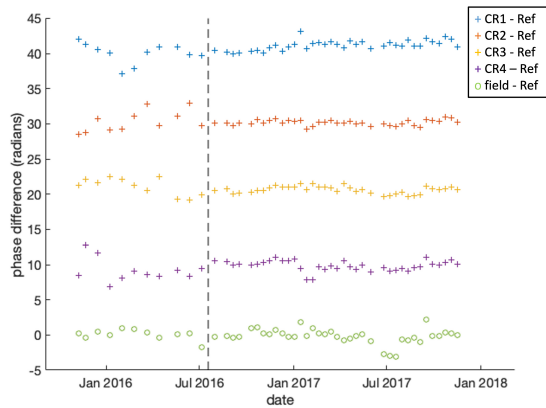
Fig. 6. Phases differences between the four corner reflectors installed around the town of Kulcs in Hungary and a nearby reference point recorded with the 051D descending track of Sentinel-1 (blue, red, yellow, and purple time series). Green dots show the phase difference between a randomly selected ("noisy") point in the area and the same reference point. Vertical dashed line shows the time of the installation of the reflectors.
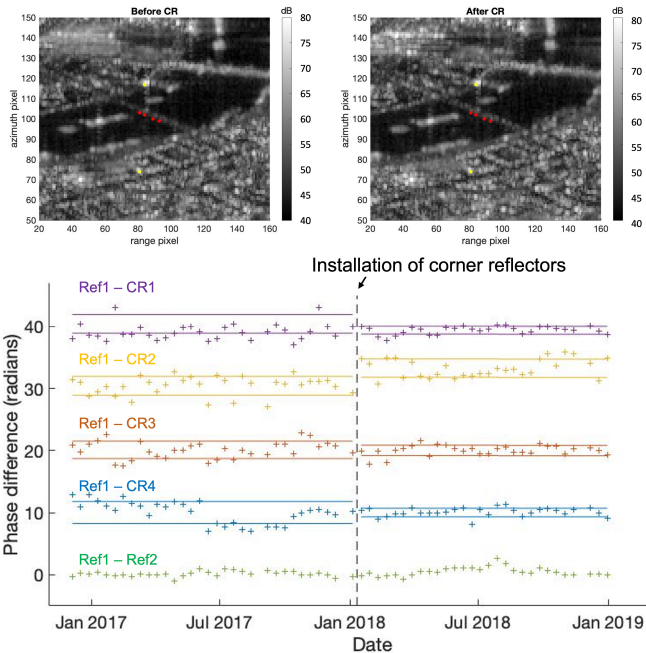

Fig. 7. Results of Sentinel-1 ascending data processing over the Waterloo Bridge in London. Top left and top right panels show the InSAR amplitudes before and after installation of the 0.35-m corner reflectors, respectively. Red dots mark the locations of the corner reflectors and yellow dots the locations of the selected reference points. The bottom panel shows the phase differences before and after the installation of the corner reflectors compared with the nearby reference point south of the bridge. Horizontal lines mark +/− standard deviation from the mean phase difference.
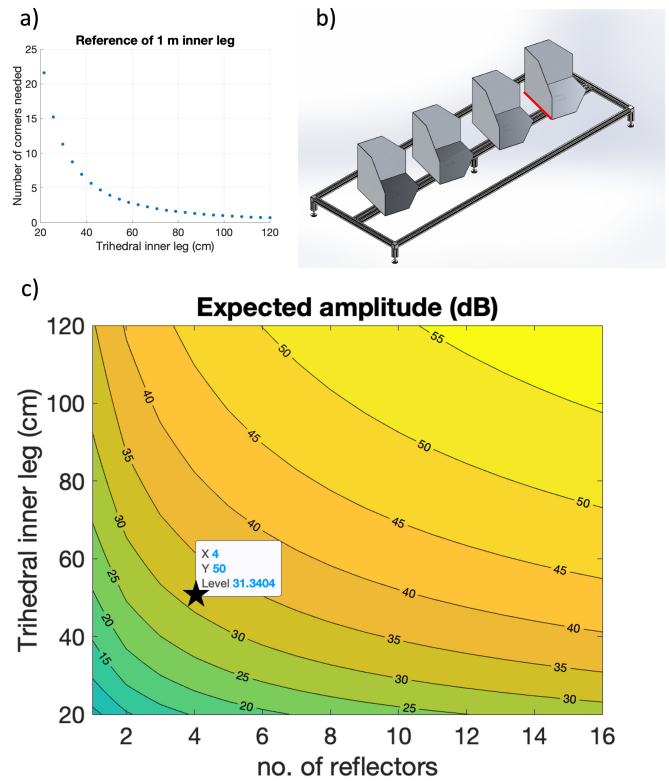

Fig. 8. (a) Distribution of the size and number of corner reflectors needed to achieve the same SCR with a reference of a trihedral corner reflector with a 1-m-long inner leg. (b) Design plan of the four corner reflector arrays. Red line shows the corner reflector inner leg measure. (c) Expected amplitude in dB depending on the size and number of triangular trihedral reflectors. The black star shows the dB value (31.3) corresponding to four reflectors with 50-cm inner leg length.

that these calculations assume the signals' sum constructively. As we discuss later, this depends strongly on the various aspects of the installation.

Following studies on the shape of a corner reflector [31], [32], we choose to use triangular trihedral corners, as it proves to be both efficient and not as sensitive to errors in the installation as other shapes. To keep the corner reflector setup as compact in projection as possible, we also truncated the outer corners of the reflectors, as this is shown to not have a measurable effect on the reflectivity of the triangular trihedral shape [13].

To carry out various experiments with the four small reflectors, we attached them to a frame, where they can be placed in a straight line, with an adjustable distance in between them. Each reflector can be rotated and tilted in any direction. A pole is attached to the frame, to which we attached a GNSS antenna for monitoring any movement of the ground below the frame. We took hour-long GNSS measurements during the morning of each day when the Sentinel 1A or 1B satellites acquired data over the area.

We also manufactured a large corner reflector with 1.5-m inner leg which was placed on the same field for reference. This was also a truncated trihedral with an actual inner leg length of 1 m. This corner reflector was set up in an "ideal" position facing the line of sight of the ascending satellite acquisition (a direction of 259° from north and a tilt of 17.3° from horizontal). We also acquired hour-long GNSS measurements at this reference reflector at the same time as at the frame of the small reflector. We set up the reflectors on the 9th of November 2020, at University of Leeds Farm, located between Leeds and York in the U.K. (Fig. 9). The exact coordinates of the reference reflector are 53.8658 N, 1.3337 W, and of the four-corner array are 53.8658 N, 1.3322 W. Fig. 10 shows the photographs of the installation of the corner reflectors.

The area of the farm is covered by two ascending Sentinel-1 tracks; we aimed the reflectors toward track 132. Using
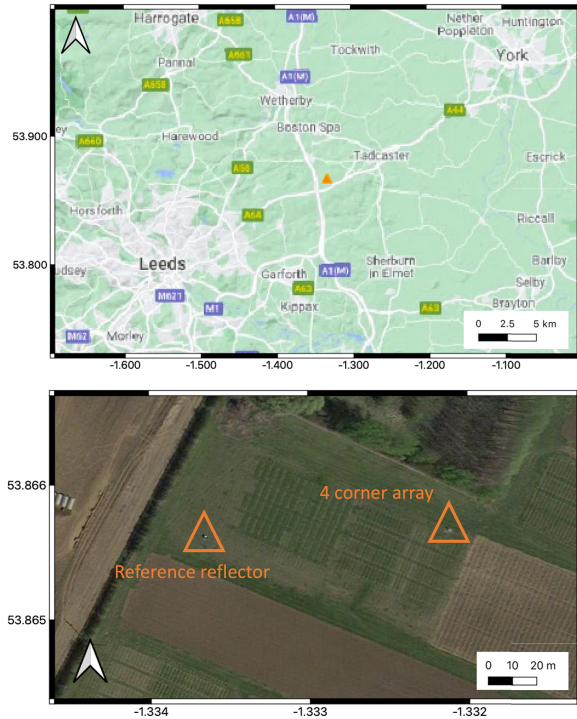
Fig. 9. (Top) Location of the test site between Leeds and York. (Bottom) Positioning of the corner reflectors on the farm test site. Source: Google Map and Google Satellite.

Fig. 10. Photographs of the installation of the various configurations. (Top Left) Alignment in range horizontal. (Top Right) Alignment in azimuthal horizontal. (Bottom Left) Alignment in azimuth vertical. (Bottom Middle) Same vertical alignment with shadowing (where the vertical separation is too small to have a clear view of the satellite for the lower three reflectors). (Bottom Right) Large reflector intended as a reference reflector in the field.

both the Sentinel-1A and 1B InSAR acquisitions, we obtained measurements every six days at around 17:50 local time.

B. InSAR Results

We installed the reflector array in various configurations, aligning them in range, azimuth, and an arbitrary direction in horizontal setups, as well as aligning them vertically (Fig. 10). We also experimented with a "shadowed" setup where within a vertical setup we moved the four corner reflectors closer

to each other. In this case, the lower three reflectors do not have a clear line-of-sight vision of the satellite for the whole area of the reflector. A full list of the various setups and the corresponding dates are shown in Table IV in the Appendix. The alignments in azimuth and range of the frame were obtained using both a compass and a GNSS reference line. The individual corner reflector tilts were measured with a digital inclinometer. During the time of the experiment, the local magnetic declination according to the World Magnetic Model [33] was between $0.35°$ and $0.45°$ ($\pm 0.4°$) and was not taken into account when orienting the corner reflector array. Alignment requirements are further discussed in Section IV-A.

We processed the Sentinel-1 data using the GAMMA-based LiCSAR package as described in Section II-C between July 2020 and May 2021. We did not apply any multilooking to preserve the natural resolution of the acquisition. The amplitudes of coregistered SLC images over the area of the farm are shown in Fig. 11. The amplitude values are averaged over the four months before the installation of the corner reflectors (1st July 2020 to 5th November 2020) and during the azimuthal alignment setup (29th November 2020 to 4th January 2021).

We extracted the amplitude values for the duration of the experiment from the coregistered SLC images corresponding to the pixels where the reflector array and the reference corner reflector were placed. To find the exact phase and amplitude center of the experimental setup and of the reference corner reflector, we oversampled a subset of the SLC images 16 times. Oversampling gives better point density, and therefore we could more accurately pinpoint the phase center of the reflectors [34], [35]. For the reflector array, the oversampled pixel position changes between different setups, but stays the same within each individual setup. We also selected a further two pixels for amplitude and phase analysis: a reference pixel corresponding to a nearby cluster of buildings and a background "field" pixel corresponding to the grassy field between the location of the large corner and the reflector array. Fig. 12 shows the amplitude time series before and during the experiment for the selected four pixels: Reference reflector (blue), four-corner reflector array (red), reference building (yellow), and background field (purple).

The vertical lines on Fig. 12 separate the various setups of the four-corner reflector array, while horizontal lines show the expected amplitudes for different cases. We calculated the large reference reflector to have a nominal RCS of 38.38 dB, and the array of four corners 31.34 dB without any shadowing and 28.8 dB with the setup where there is shadowing in the vertical direction 3. We find that the large reflector has an amplitude as expected, except for a dip on 22nd May 2021. This was due to water accumulation in the reflector; we manufactured the reflector with a small hole in the middle for drainage, but on this occasion the hole was filled with debris and had to be manually removed. The amplitude of the four-corner array exceeded our expectations both with and without shadowing, perhaps due to the contributions from the frame.

We processed the hour-long GNSS measurements with the GAMIT/GLOBK GNSS processing package, using the closest
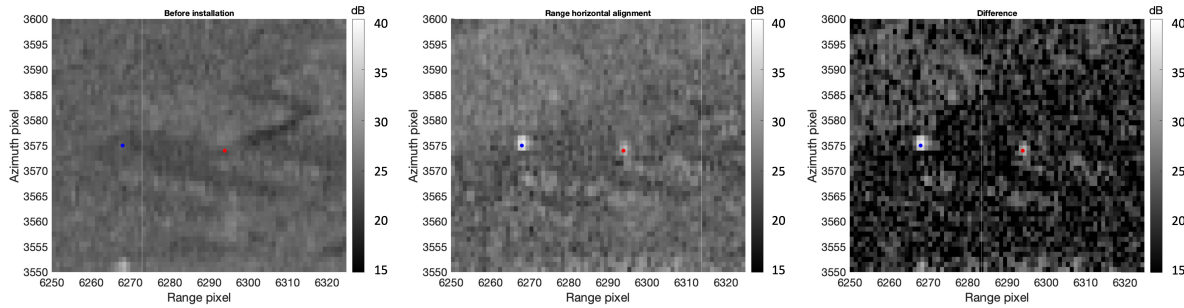
Fig. 11. Amplitudes of coregistered SLC images over the area of the farm. (Left) Before installation (average over 1st July 2020 to 5th November 2020). (Middle) During the range horizontal alignment setup (average over 29th November 2020 to 4th January 2021). (Right) Difference between the left and middle panels. Blue dot marks the location of the large reference reflector, and red dot marks the location of the four-corner reflector array.
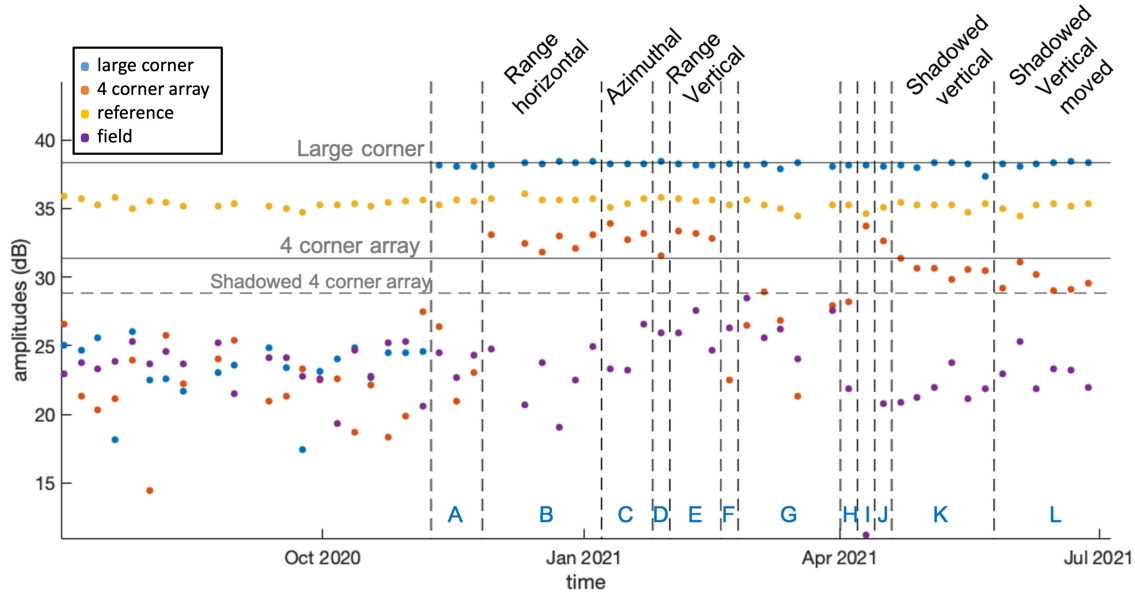

Fig. 12. Amplitudes of individual pixels extracted from the coregistered SLC images: reference reflector (blue), four-corner reflector array (red), reference building (yellow), and background field (purple). Vertical lines separate the various setups of the four-corner reflector array, while horizontal lines show the expected amplitudes for different cases. Letter codes of each setup are explained in detail in the Appendix (Table IV).

TABLE II

COHERENCE VALUES AND STANDARD DEVIATIONS OF THE PHASE SIGNAL CONVERTED INTO DISPLACEMENT OF THE VARIOUS SETUPS OF THE CORNER REFLECTOR ARRAY. NOTE THAT THE "REFERENCE-LARGE CORNER" AND "REFERENCE-FIELD" SETUPS DO NOT CHANGE OVER TIME. THE LETTERS REFER TO THE CORRESPONDING SETUPS ON FIGS. 12 AND 13. FOR THE FULL LIST OF SETUPS, SEE TABLE IV IN THE APPENDIX

Letter code	setup	no. of points	Reference - - 4-corner array		Reference - - Large corner		Large corner - - 4-corner array		Reference - - field		Start date
			coh	std (mm)	coh	std (mm)	coh	std (mm)	coh	std (mm)	
	Before	10	0.32	9.41	0.51	10.16	0.39	5.78	0.46	5.75	2020-09-12
B	Range hor.	6	0.98	0.98	0.87	2.47	0.93	1.67	0.47	5.25	2020-11-29
C	Azimuthal	3	0.80	12.75	0.78	3.69	0.90	2.40	0.80	3.56	2021-01-10
E	Range Vertical	3	1.00	0.33	0.99	0.62	1.00	0.40	0.85	3.01	2021-02-09
K	Shadowed Vert.	6	0.95	1.63	0.93	1.88	0.98	0.99	0.17	8.65	2021-04-22
L	Shadowed Vert. Moved	6	0.87	2.33	0.92	1.77	0.99	0.63	0.43	7.08	2021-05-28

permanent GNSS station as a reference point [36]. This station (LEED) is managed by the NERC British Isles continuous GNSS Facility (BIGF). There was no movement of the ground during the time of the experiment that would measure above the noise level of the acquired GNSS data (∼1–2 mm). We also did not measure any settlement of the corner reflectors during the experiment and within the various setups. Detailed GNSS results are shown in Appendix C.

We carried out the phase analysis using the same four pixels selected (reference corner, four-corner array, reference

building, and background field). Fig. 13 shows the phase differences between these pixels before and during the time of the experiment.

To quantify the phase noise, we analyzed the coherence of each setup using the following equation (7) from (16) in Pepe and Lanari [37]:

$$\gamma = \frac{\left|\sum_{p=0}^{M-1} \exp\left[j\left(\varphi_p - \bar{\varphi}_p\right)\right]\right|}{M}, \qquad 0 \leq \gamma \leq 1 \qquad (7)$$
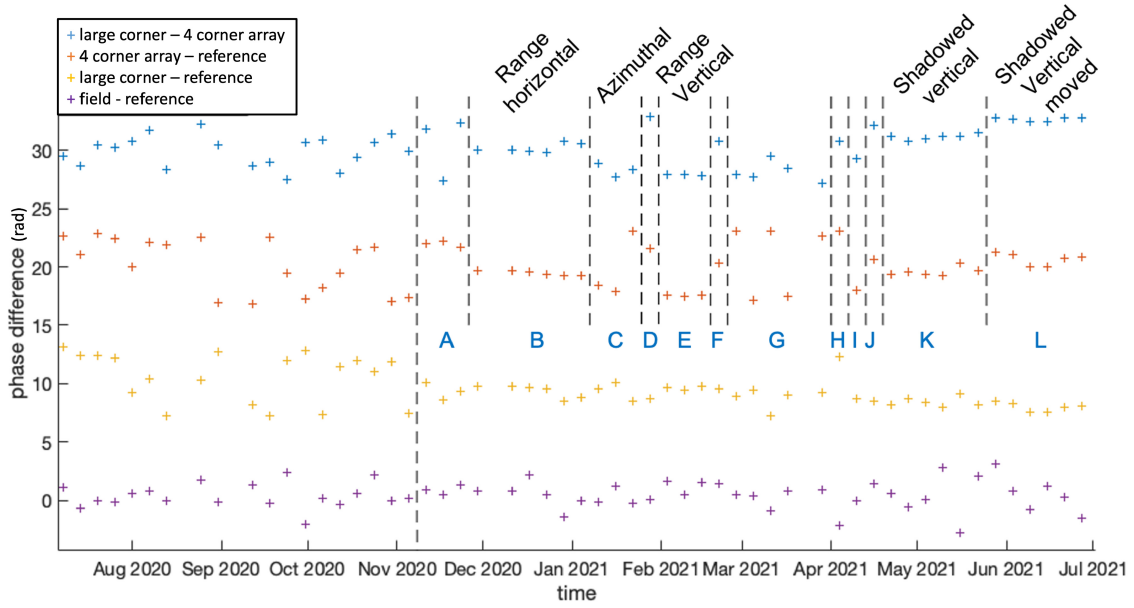
Fig. 13. Phase differences between the four selected pixels: reference corner, four-corner array, reference building, and background field. Vertical lines separate the various setups of the four-corner reflector array. Letter codes of each setup are explained in detail in the Appendix (Table IV).
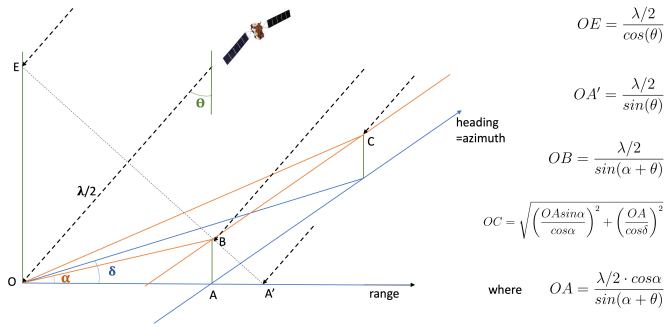

$$OE = \frac{\lambda/2}{cos(\theta)}$$

$$OA' = \frac{\lambda/2}{sin(\theta)}$$

$$OB = \frac{\lambda/2}{sin(\alpha + \theta)}$$

$$OC = \sqrt{\left(\frac{OAsin\alpha}{cos\alpha}\right)^2 + \left(\frac{OA}{cos\delta}\right)^2}$$

where $$OA = \frac{\lambda/2 \cdot cos\alpha}{sin(\alpha + \theta)}$$

Fig. 14. Distance between corner reflectors to achieve constructive interference. Blue lines mark a horizontal plane, and orange lines mark a plane tilted by α. Reflectors placed at positions E, A', B, or C will constructively interfere with a reflector in position O. Calculation of distances is based on the Sentinel-1 half wavelength ($\lambda/2$), incidence angle (θ), tilt from horizontal (α), and angle from azimuth in the horizontal plane (δ).
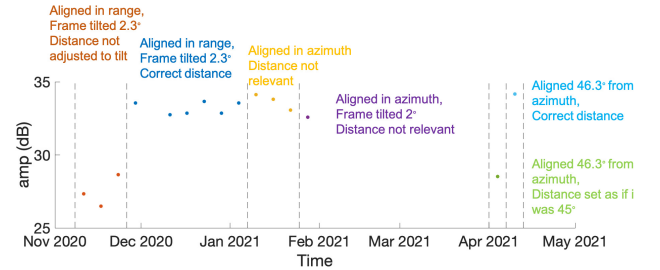

Fig. 15. Examples of importance of small adjustments: Orange and blue points show a frame aligned in the horizontal range direction, with and without a 2.3° tilt from optimal, respectively. Yellow and purple points show a frame aligned in the azimuthal direction, where distances are irrelevant, with a correctly tilted frame and a 2° over-tilted frame, respectively. Green and blue points show a frame rotated 46.3° from azimuth, with distances adjusted for a 45° and a 46.3° rotation, respectively.

calculating the γ coherence for each setup using the M number of measurements and $j(\varphi_p - \bar{\varphi}_p)$ phase difference between the reference epoch and all other measurement epochs corresponding to each setup. Table II shows the results of these calculations for each setup between different locations.

Based on the phase and coherence analysis, we find that the phase signal of the four-corner array is stable in the horizontal range alignment and each vertical alignment. In the horizontal azimuth aligned configuration, the phase appears less stable, and the coherence values are lower, but we do not have enough data points to draw this conclusion.

C. Controlled Movement

During the last setup of the four-corner experiment we kept the shadowed vertical setup and moved each of the corner reflectors approximately 5 mm upward along the vertical rail. We measured the phase difference between the four-corner array and the reference reflector during the six acquisitions before this movement and during the six acquisitions after the movement (K and L setups in Figs. 12 and 13). The mean phase difference of 1.24 rad in the line-of-sight direction corresponds to a 6.9-mm movement in the vertical direction, which we consider within the error of our movement accuracy.

IV. PRACTICAL CONSIDERATIONS

A. Constructive Interference

Achieving constructive interference between the reflectors is essential. One of the most important factors is spacing between the reflectors, which matters when they are aligned in the range direction, while it can be anything when aligned in the azimuthal direction. Fig. 14 shows how distances can be calculated depending on which configuration the reflectors are placed. It is important to keep in mind that a small error in tilt or orientation can significantly affect the optimal distance between the reflectors. The distance between corner reflectors

refers to the distance between the reflecting centers rather than the distance between the physical center of the reflectors. We used sub-mm precision when setting the distance during our experiments with the four-corner array.

Fig. 15 demonstrates two examples of the importance of small deviations of the ideal orientations and the effect on the amplitude if the distance between the corner reflectors is not adjusted. The ideal tilt of each reflector was 17.3° at the location of the farm where the experiment was set up. Destructive interference due to tilting is demonstrated by a setup where we tilted the frame 2.3° to which the reflectors are attached (α in Fig. 14). However, in the first instance the distance between the reflectors was kept as if the frame was horizontal (OA' in Fig. 14, orange datapoints in Fig. 15). In the next setup, we adjusted the distance between the reflectors so that the 2.3° tilt of the frame is taken into account (OB in Fig. 14, dark blue datapoints in Fig. 15).

The second example relates to a setup where we rotated the frame 46.3 ° from the azimuth direction in the horizontal plane (δ in Fig. 14). As in the previous case, the frame was tilted 2.3° from horizontal so that the individual reflectors have a 17.3° tilt from horizontal (OC in Fig. 14). At first, the distance between the reflectors was set to account for a 45° rotation and the 2.3° tilt of the frame (green datapoint in Fig. 15). In the following setup, we adjusted the distance to account for a 46.3° rotation rather than a 45° one. As shown in Fig. 15 with the light blue datapoint, a miscalculation in the distance relating to a 1.3° rotation causes destructive interference.

These two examples show that a 2° tilt of the frame and a 1.3° rotation of the frame can cause significant destructive interference between the reflectors, if the distances between them are not carefully adjusted. This leads to great loss of amplitude. Some parameters are less sensitive than others, for example, if the reflectors are aligned in the azimuthal direction, the distance between them is irrelevant (BC in Fig. 14, yellow datapoint in Fig. 15). As an experiment, we tilted the frame another 2°, setting up a 19.3° tilt, and find that the amplitude of the measurement did not significantly decrease (purple datapoint in Fig. 15).

During the experiments with the vertical setup, we moved the reflectors closer to each other so that they shadow each other to see the effect on the amplitude, phase, and coherence. We found that while the amplitude decreases as the overall area of reflecting surfaces decreases, the phase and coherence remain stable. While shadowing between the reflectors is not ideal, if the overall projection of the array needs to be reduced, it can be done at the cost of minimal amplitude reduction. The size of the reflector can also be optimized to take advantage of the resonance maxima. The RCS equations shown in this article work in the optical region, but not in the Rayleigh region. Using the RCS equations that apply in the Mie region in between these two, it is theoretically possible to achieve higher than expected RCS [38].

In the course of six months of the experiment, and during the various seasons, we observed that snow, debris, rain, or bird droppings can accumulate in the corner reflectors and can cause a loss of amplitude when not removed on time. We found that the hole in the corner that we cut for drainage is too small when debris accumulates and can cause rainwater to accumulate. A larger hole could solve this problem, or a cover on the corner reflector that would protect it from rain and larger leaves and other debris falling in. This cover would have to let the SAR waves through not to lose the signal.

B. Optimal Arrangement

The horizontal alignment in azimuth is ideal in that the spacing between reflectors does not matter, and an array can therefore be produced with a fixed spacing that is suitable for multiple applications. However, the spacing can also be fixed with an alignment in range, with the spacing set for an average incidence angle. The whole array can then be tilted to account for the actual incidence angle at the installation location. This will result in a nonideal orientation for each individual reflector, but a tilt of a few degrees does not significantly affect the RCS.

On the side of structures, such as bridges or tall buildings, a vertical setup would be ideal, while on the top of structures or along embankments a horizontal setup is more desirable. Bespoke arrays can be designed for the sides of nonvertical structures.

V. Conclusion

In this article, we present a novel corner reflector array of four small reflectors that can replace a large one and provide equivalent amplitude, phase, and coherence in InSAR applications. It is especially useful in urban areas to monitor essential infrastructure remotely.

We analyzed the Sentinel-1 InSAR data acquisitions over corner reflectors of various sizes. We found that to observe a distinct amplitude signal with the C-band Sentinel-1 InSAR measurements, an inner leg of a triangular trihedral reflector needs to be at least 1 m long. We observed that an inner leg of 0.6 m is too small to give a consistently large amplitude to stand out from the background and stable phase signal; but have not established a clear cut-off in between, as we did not process any data over corner reflectors that have an inner leg length between 0.6 and 1 m. The theoretical considerations discussed in Section II-A show that the sufficient size of the corner reflector depends both on the wavelength of the SAR acquisition and the background clutter level of the area of interest. The corner reflector can be truncated as shown by [13] and the 1-m inner leg can be reduced to 0.67 m while still achieving similar amplitudes.

Due to its size, a corner reflector projecting 0.67 m may still be too large to be routinely used in urban areas for essential infrastructure monitoring. In some places, there are restrictions on the projection and size of external fixtures (e.g., 30 cm on Waterloo Bridge in London), while in other places it would just not be feasible to place such an object, or it would attract too much unwanted attention. We propose to replace

one corner reflector with an array of smaller ones within the same SAR resolution cell. We designed and manufactured an array of four corner reflectors, each of them with a truncated inner leg of 0.33 m, equivalent to a 0.5-m triangular trihedral corner reflector. When placed in the same pixel, their signals combine as if they were a single 0.67-m truncated or equivalent 1-m triangular trihedral corner reflector. With various setups in the azimuthal, range direction, vertical, and arbitrary alignments, we show that the four-corner array meets the expectations of predicted amplitude signal and gives a stable and coherent phase signal over multiple acquisitions. Through the various setups of the experiment, we demonstrated that it is essential that the distance between the corner reflectors is adjusted carefully (to the mm) in the range horizontal and vertical planes to achieve constructive interference between the reflectors.

We used the array of four corner reflectors as an example, but depending on the exact application and location of placement, in theory any number of reflectors can be used in any 2-D or 3-D configuration, as long as the distance between them is set up to achieve constructive interference, and shadowing of one reflector by another is avoided.

There are numerous potential applications of corner reflector arrays in urban areas. Monitoring essential infrastructures, such as bridges, flyovers, and transport systems, is becoming ever more difficult with the rapid expansion of urban areas. It is also important to survey short- and long-term effects of newly built tunnels and railway embankments, and observe subsidence and other ground-motion related changes in critical buildings in urban areas. Often the object or infrastructure of interest does not give sufficient amplitude in SAR images or lack distinct points in space that can be associated with the SAR signal. In these cases, a corner reflector array that is installed as an external fixture or already contained as features in newly built structures can provide an important tool in remote monitoring of these structures. The Sentinel mission is providing reliable and free SAR data with revisit times of 6–12 days in either ascending or descending configuration. Therefore, long-term accurate motion can be established using a reflector array that can highlight seasonal variations and alert to changes in ground stability.

APPENDIX A
AMPLITUDE AND PHASE IMAGES OF THE VARIOUS CORNER REFLECTORS

See Figures 16–31.

APPENDIX B
COHERENCE OF THE VARIOUS CORNER REFLECTORS

In this section, we refer to the corner reflectors in Table I.

We analyzed the coherence of the corner reflectors at various locations using (7) from (16) in Pepe and Lanari [37]. calculating the γ coherence for each setup using the M number of measurements and $j(\varphi_p - \bar{\varphi}_p)$ phase difference between the reference epoch and all other measurement epochs corresponding to each setup (Fig. 32).

For each corner reflector, we used ten acquisitions, as close to the installation date as possible with the varying availability of the Sentinel-1 measurements. In some cases when the corner reflectors were installed years before the start of the Sentinel mission and their size is not larger than an inner leg length of 0.6 m, it is not possible to say whether we chose the right pixel for the coherence analysis. This clearly shows in the large spread of coherence values and no clear increase with size that we see with the corner reflectors with sizes between 0.3 and 0.6 m. The corner reflectors with a 1-m inner leg length (both trihedrals and truncated trihedrals) show a coherence close to 1, with some outliers down to a coherence of 0.6. We do not know whether there was any real movement of the corner reflectors recorded during this time, and therefore cannot subtract any such movement during the coherence analysis. In conclusion, the coherence of the corner reflectors with a 1-m inner leg length seems satisfactory for further analysis.

Table III shows the standard deviation values for the phase differences where acquisitions were available both before and after the installation of corner reflectors.

APPENDIX C
RESULTS OF THE GNSS MEASUREMENTS

In this section, we show the results from the GNSS measurements that we carried out every six days. These hour-long measurements took place on the days when the Sentinel-1 track 132 acquisitions were made. We processed the GNSS data with the GAMIT/GLOBK GNSS processing package, using the closest permanent GNSS station (LEED) as a reference point [36].

Between the different setups, we occasionally repositioned the antenna, to ensure it was not in the SAR line of sight. Large movements on the antenna between setups are due to this manual repositioning.

Within each setup (described in Table IV), we calculated the difference between the position of the reference corner reflector and the four-corner array. Between the setups, we moved the array and adjusted the position of the GNSS antenna depending on the horizontal or vertical setup; this can be observed in the GNSS results shown in Fig. 33. However, within a single setup we find that there was no movement of the ground that would measure above the noise level of the acquired GNSS data (∼1–2 mm), with the exception of the north component within setup C. This seems to be an outlier as we do not expect any ground motion occurring on the farm, and it is probably due to an atmosphere related error. We also did not measure any settlement of the corner reflectors during the experiment and within the various setups.

APPENDIX D
SUMMARY OF THE VARIOUS SETUPS AND THE CORRESPONDING DATES
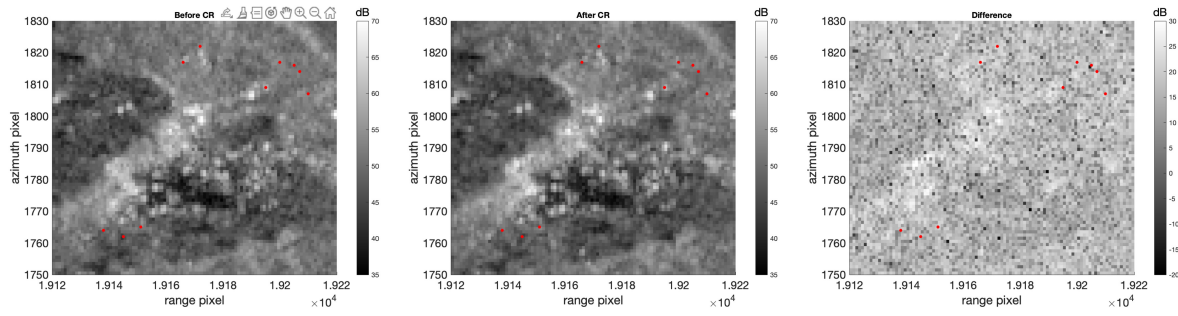
See Tables III and IV.

Fig. 16. Average amplitudes of corner reflectors at the Pisciotta area 1, Italy, recorded by the 044A ascending track. Red dots mark pixels with a reflector placed there. Corner reflectors are 0.6-m trihedrals.
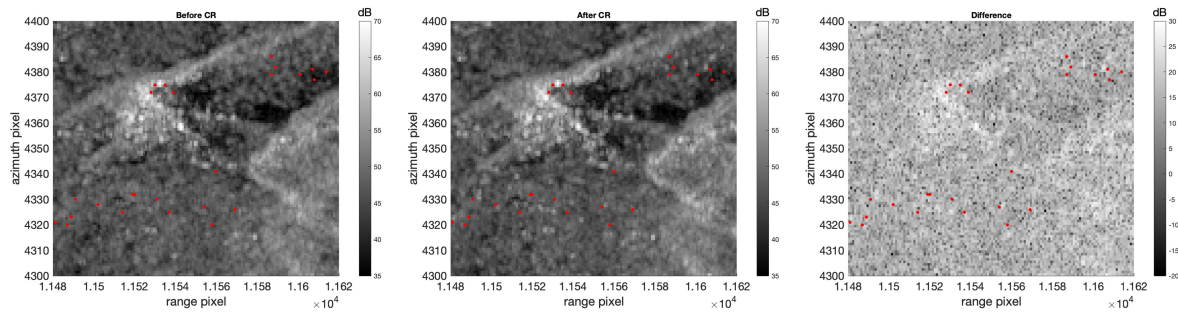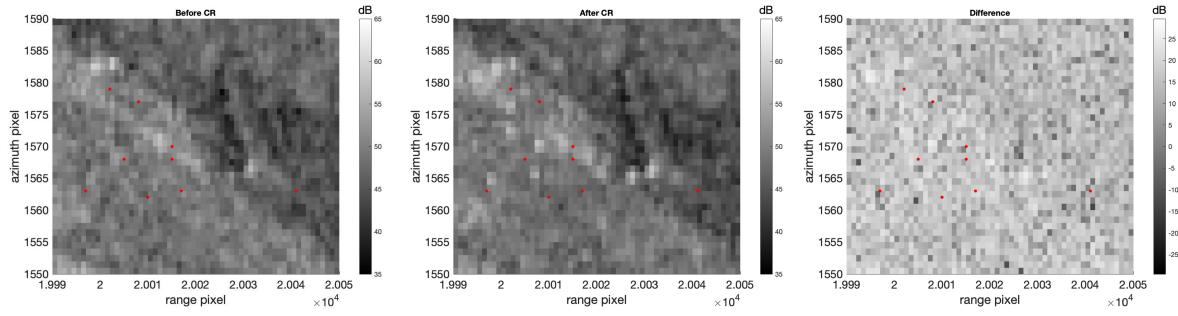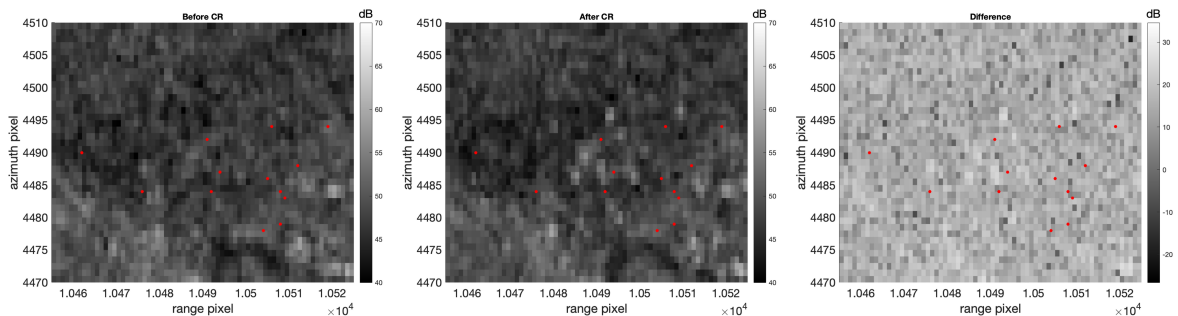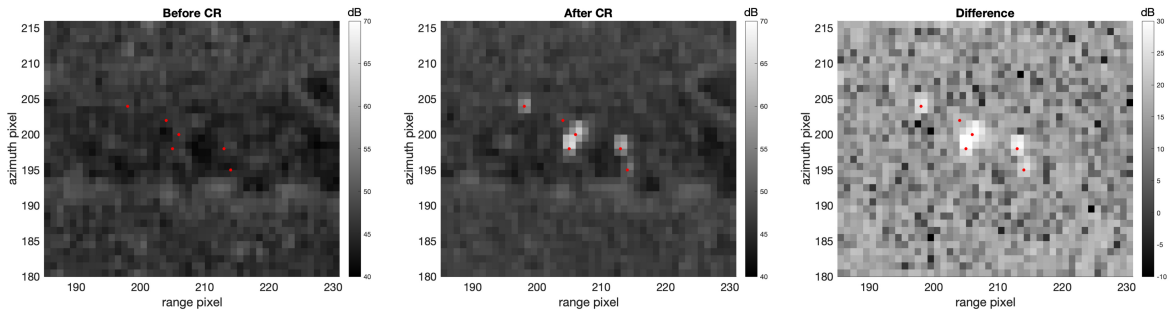

Fig. 17. Average amplitudes of corner reflectors at the Pisciotta area 1, Italy, recorded by the 124D descending track. Red dots mark pixels with a reflector placed there. Corner reflectors are 0.6-m trihedrals.

Fig. 18. Average amplitudes of corner reflectors at the Pisciotta area 2, Italy, recorded by the 044A ascending track. Red dots mark pixels with a reflector placed there. Corner reflectors are 0.6-m trihedrals.

Fig. 19. Average amplitudes of corner reflectors at the Pisciotta area 2, Italy, recorded by the 124D descending track. Red dots mark pixels with a reflector placed there. Corner reflectors are 0.6-m trihedrals.

Fig. 20. Average amplitudes of corner reflectors at the Hollin Hill landslide recorded by the 132A ascending track. Red dots mark pixels with a reflector placed there. Corner reflectors are 1-m truncated trihedrals.
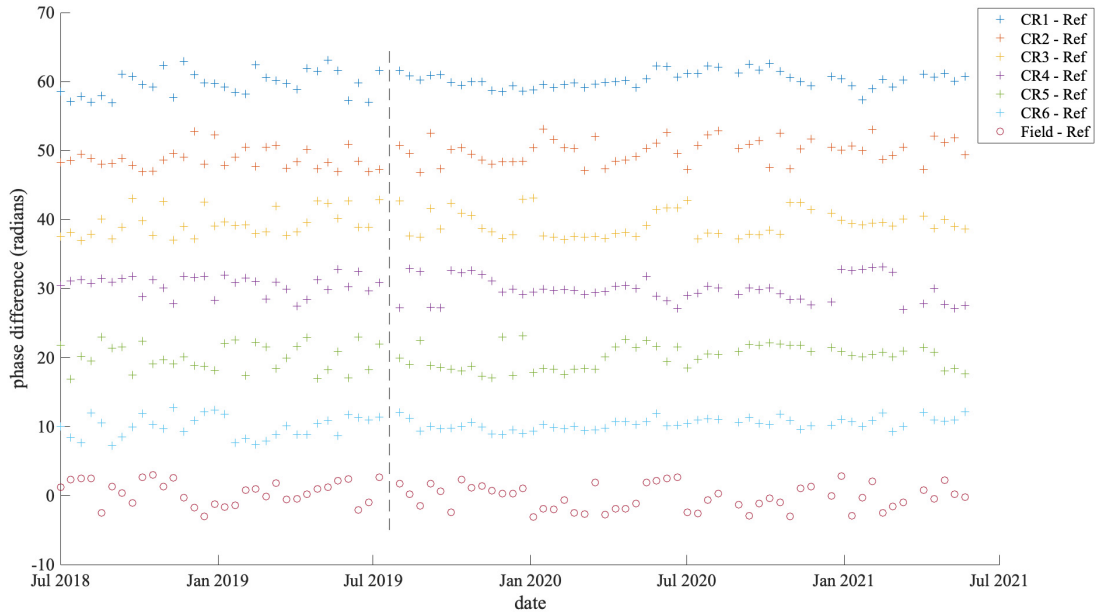

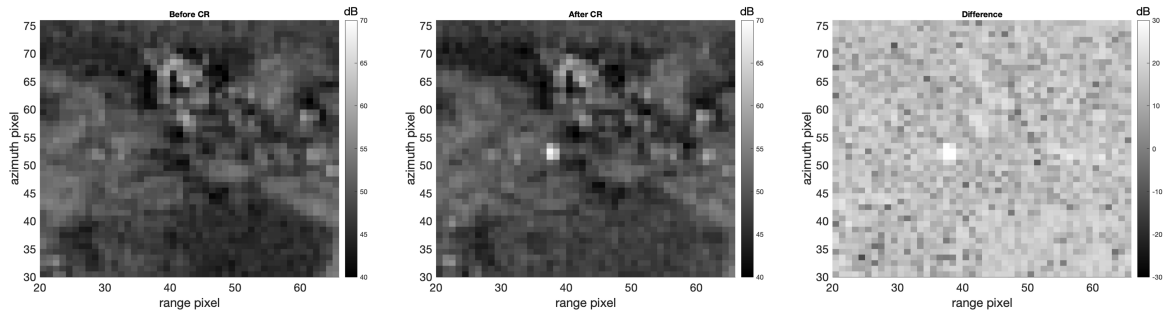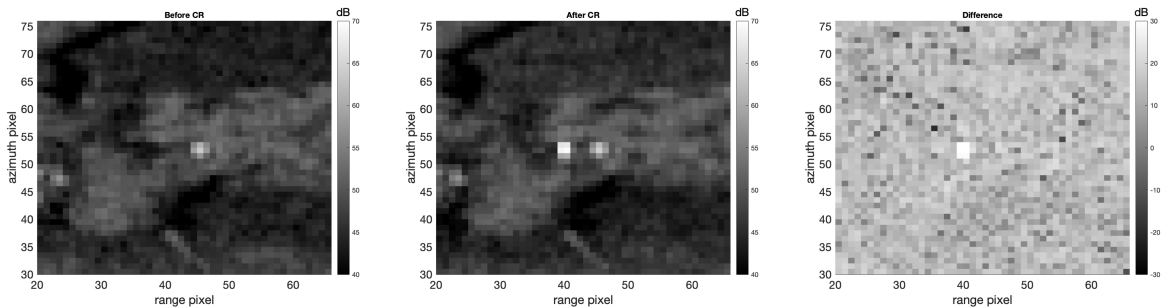Fig. 21. Phase differences of corner reflectors and a nearby reference point at the Hollin Hill landslide.

Fig. 22. Average amplitudes of the corner reflector at the Herstmonceux site, U.K., recorded by the 081D descending track. Corner reflectors are 1-m truncated trihedrals.

Fig. 23. Average amplitudes of the corner reflector at the Herstmonceux site, U.K., recorded by the 132A ascending track. Corner reflectors are 1-m truncated trihedrals.
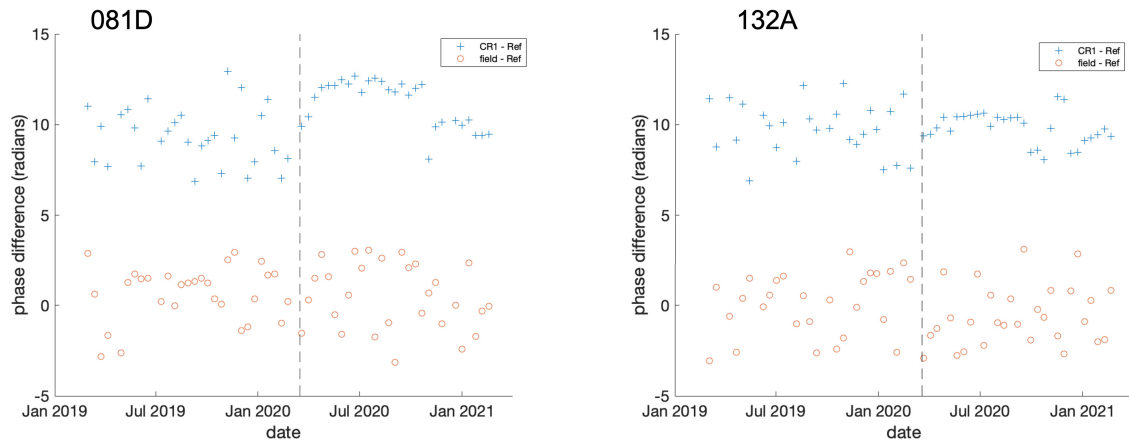
Fig. 24. Phase differences of the 081D descending (left) and 132A ascending (right) facing reflectors and a nearby reference point at the Herstmonceux site, U.K.
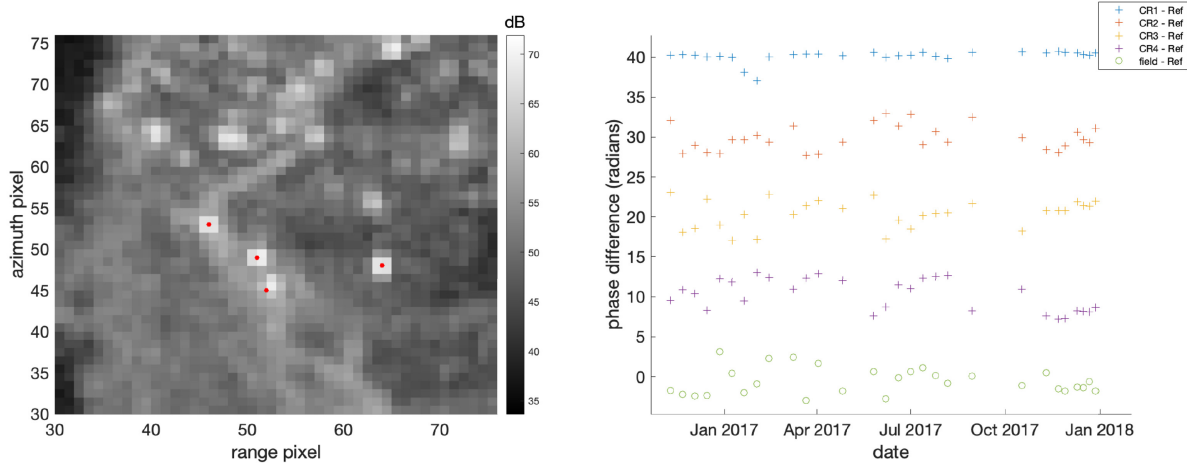

Fig. 25. (Left) Average amplitudes of corner reflectors at the Dunaszekcso area in Hungary landslide recorded by the 051D descending track. Red dots mark pixels with a reflector placed there. Corner reflectors are 1-m truncated trihedrals. (Right) Phase differences of corner reflectors and a nearby reference point at the Dunaszekcso area in Hungary.
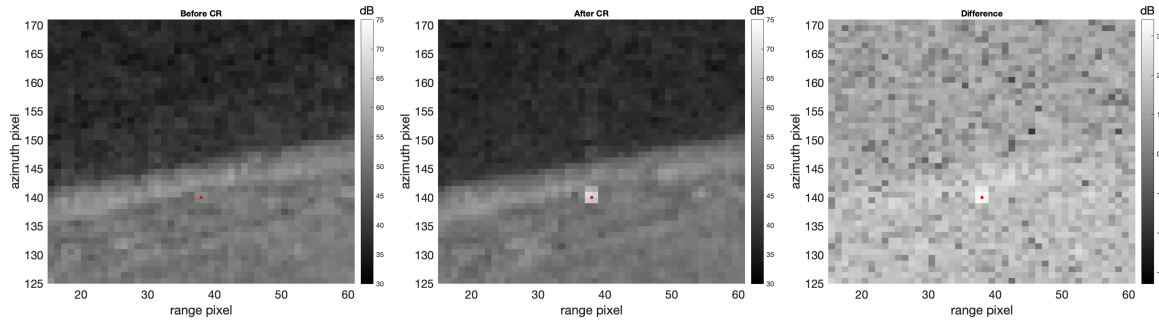

Fig. 26. Average amplitudes of one of the corner reflectors at the Fonyod area in Hungary recorded by the 073D descending track. Red dots mark pixels with a reflector placed there. Corner reflectors are 1-m truncated trihedrals.
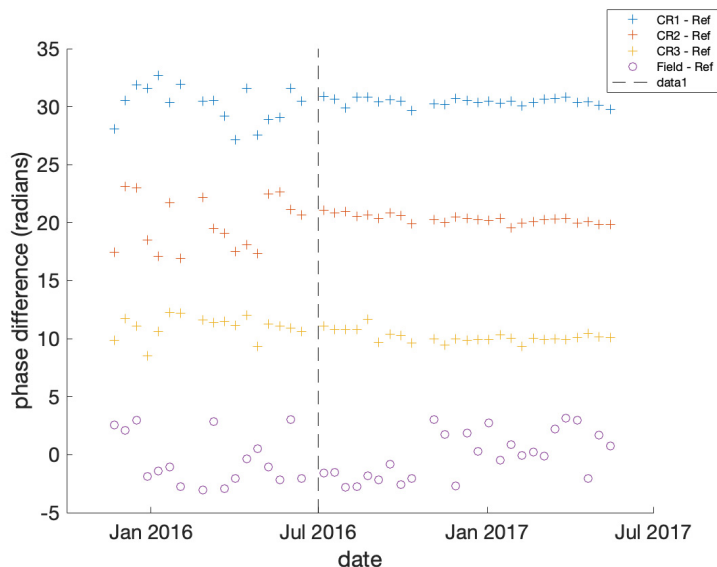
Fig. 27. Phase differences of corner reflectors and a nearby reference point at the Fonyod area in Hungary.
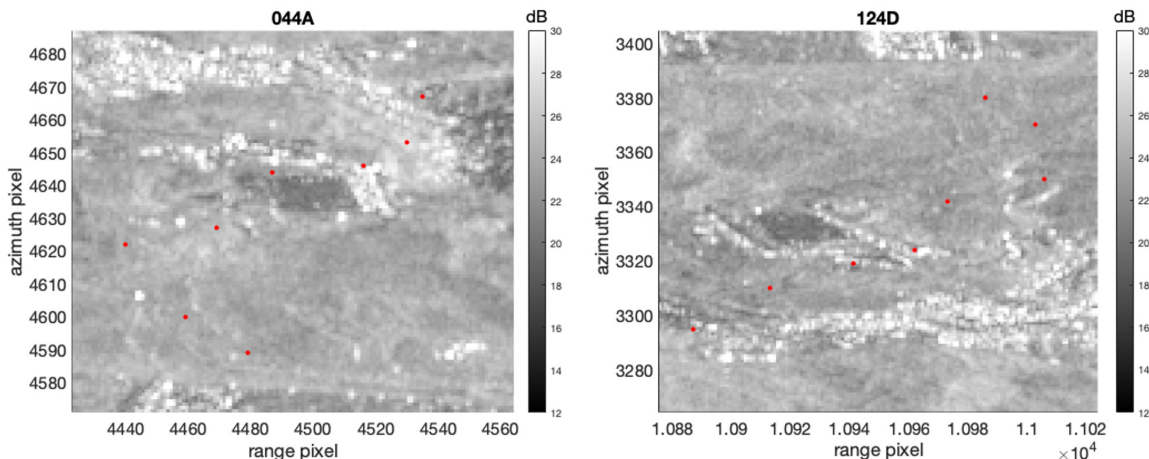

Fig. 28. Average amplitudes of the Calitri area in Italy recorded by the 044A ascending and 124D descending tracks. Red dots mark pixels with a reflector placed there. These reflectors have been installed in 2008 and their status is unknown at the time of start of the Sentinel-1 mission in 2014. Corner reflectors are 1-m trihedrals.
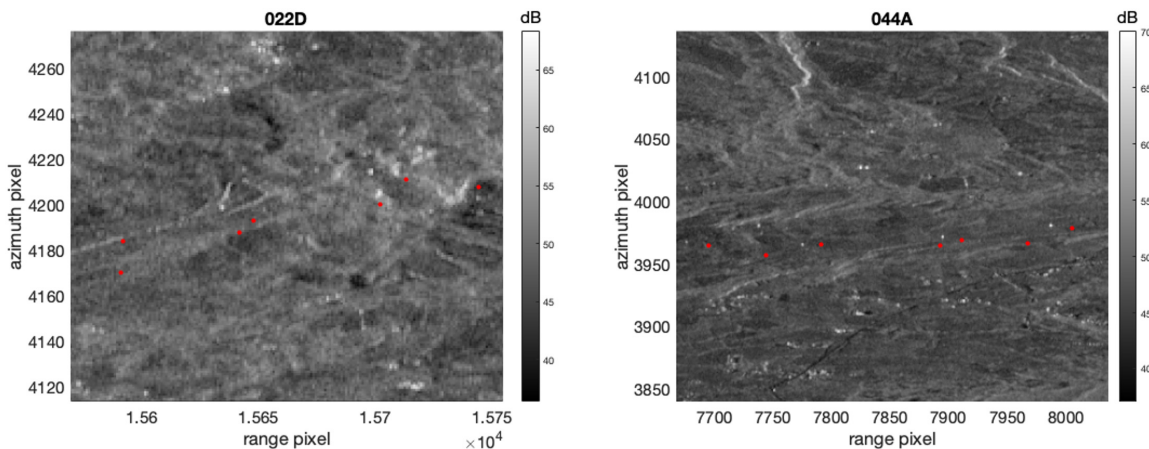

Fig. 29. Average amplitudes of the Agnone area in Italy recorded by the 022D descending and 044A ascending tracks. Red dots mark pixels with a reflector placed there. These reflectors have been installed in 2009 and their status is unknown at the time of start of the Sentinel-1 mission in 2014. While some bright spots appear on the 044A image, it is unclear whether they do not correspond to the location of the red dots because of a geocoding error, or whether they are not in fact corner reflectors but other built structures with a bright SAR signal. Corner reflectors are 1.4-m trihedrals.
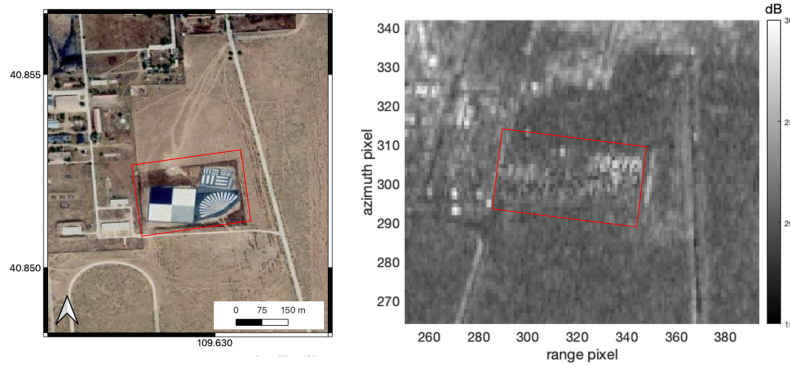
Fig. 30. (Left) Aerial photograph of the bar pattern installed for testing various X and C band InSAR satellite acquisitions. (Right) Average amplitudes of the bar pattern area in China recorded by the 011A ascending track. Red rectangles show the areas corresponding to the bar pattern.
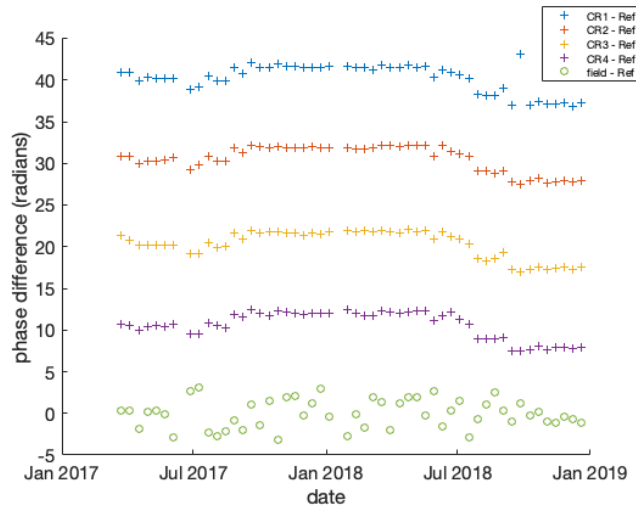

Fig. 31. Phase differences of bright points among the bar pattern (marked as CR1-4) and a nearby reference point.

TABLE III

STANDARD DEVIATION VALUES OF PHASE DIFFERENCES BETWEEN THE PIXEL CONTAINING A CORNER REFLECTOR AND A REFERENCE PIXEL BEFORE AND AFTER THE INSTALLATION OF THE REFLECTORS. WHEN A LOCATION HAS MULTIPLE CORNER REFLECTORS, THE MEAN VALUE IS SHOWN IN THIS TABLE

Location	size	std before	std after	no. of reflectors
Waterloo Bridge (UK)	0.35 m	1.36	1.13	4
Kulcs (Hungary)	1 m	1.14	0.65	4
Fonyód (Hungary)	1 m	1.43	0.48	3
Herstmonceux (UK)	1 m	2.11	0.29	1 descending
Herstmonceux (UK)	1 m	1.45	0.31	1 ascending
Hollin Hill (UK)	1 m	1.57	0.43	6

TABLE IV

EXPERIMENTS CARRIED OUT WITH THE FOUR CORNER REFLECTORS. BOLD LINES SHOW THE FAVORABLE SETUPS OF WHICH WE SHOW RESULTS IN SECTION III-B. RESULTS OF ALL SETUPS ARE SHOWN IN THE APPENDIX

| Code	Start date	No. of acq.	Setup	notes
A	2020-11-11	3	Azimuthal	tilted frame, not ideal distance
B	**2020-11-29**	**6**	**Range horizontal**	
C	**2021-01-10**	**3**	**Azimuthal**	
D	2021-01-28	1	Azimuthal	tilted frame, distance unaffected
E	**2021-01-10**	**3**	**Range vertical**	**∼ 53cm**
F	2021-02-21	1	Range vertical	destructive interference
G	2021-02-27	6	Range vertical	various experiments with 3 reflectors
H	2021-04-04	1	Horizontal in 46.3deg from azimuth direction	distance was assumed for 45deg
I	2021-04-10	1	Horizontal in 46.3deg from azimuth direction	
J	2021-04-16	1	Range vertical	∼ 49cm
K	**2021-04-22**	**6**	**Shadowed vertical**	**∼ 39cm**
L	**2021-05-28**	**5**	**Shadowed vertical, moved**	**∼ 39cm** **5mm vertical movement**
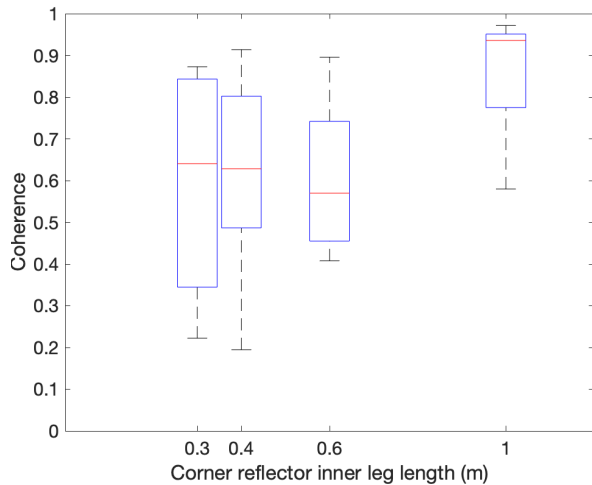
Fig. 32. Statistics of the coherence values corresponding to the various sizes of corner reflectors. Each boxplot shows the median value (red line), values within the 25th and 75th percentiles (blue box), and the minimum and maximum values (extent of dashed lines).
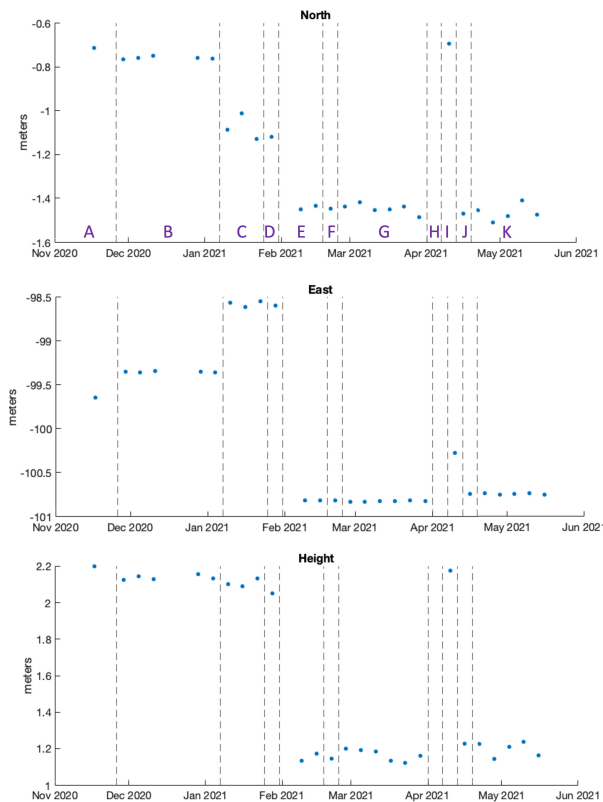

Fig. 33. Differences between the reference reflector and the four-corner array in north, east, and height.

ACKNOWLEDGMENT

REFERENCES

[1] J. Biggs and T. J. Wright, "How satellite InSAR has grown from opportunistic science to routine monitoring over the last decade," *Nature Commun.*, vol. 11, no. 1, pp. 1–4, Dec. 2020.

[2] N. Anantrasirichai, J. Biggs, F. Albino, and D. Bull, "A deep learning approach to detecting volcano deformation from satellite imagery using synthetic datasets," *Remote Sens. Environ.*, vol. 230, Sep. 2019, Art. no. 111179.

[3] T. Carlà *et al.*, "Perspectives on the prediction of catastrophic slope failures from satellite InSAR," *Sci. Rep.*, vol. 9, no. 1, pp. 1–9, Dec. 2019.

[4] J. F. Dehls, Y. Larsen, P. Marinkovic, T. R. Lauknes, D. Stødle, and D. A. Moldestad, "INSAR. No: A national InSAR deformation mapping/monitoring service in norway–from concept to operations," in *Proc. IEEE Int. Geosci. Remote Sens. Symp.*, Jul./Aug. 2019, pp. 5461–5464.

[5] Y. Morishita, "Nationwide urban ground deformation monitoring in Japan using Sentinel-1 LiCSAR products and LiCSBAS," *Prog. Earth Planet. Sci.*, vol. 8, no. 1, pp. 1–23, Dec. 2021.

[6] G. J. Funning and A. Garcia, "A systematic study of earthquake detectability using Sentinel-1 interferometric wide-swath data," *Geophys. J. Int.*, vol. 216, no. 1, pp. 332–349, Oct. 2018.

[7] M. Bakon *et al.*, "RemotIO: A Sentinel-1 multi-temporal InSAR infrastructure monitoring service with automatic updates and data mining capabilities," *Remote Sens.*, vol. 12, no. 11, p. 1892, Jun. 2020.

[8] F. Bovenga, G. Pasquariello, R. Pellicani, A. Refice, and G. Spilotro, "Landslide monitoring for risk mitigation by using corner reflector and satellite SAR interferometry: The large landslide of carlantino (Italy)," *CATENA*, vol. 151, pp. 49–62, Apr. 2017.

[9] R. Czikhardt, J. Papco, P. Ondrejka, P. Ondrus, and P. Liscak, "Corner reflector network as a geodetic reference for landslide monitoring via InSAR time series: Case study from Slovakia," in *Proc. EGU Gen. Assem. Conf. Abstr.*, Vienna, Austria, 2021, Paper EGU21-12373.

[10] D. Infante, D. Di Martire, D. Calcaterra, and M. Ramondini, "The contribution of satellite radar interferometry for land management activities," in *Proc. Int. Conf. Crit. Thinking Sustain. Rehabil. Risk Manage. Built Environ.* Springer, 2019, pp. 156–164.

[11] F. Cigna *et al.*, "25 years of satellite InSAR monitoring of ground instability and coastal geohazards in the archaeological site of Capo Colonna, Italy," *Proc. SPIE*, vol. 10003, Oct. 2016, p. 100030Q.

[12] M. Garthwaite, S. Nancarrow, A. Hislop, M. Thankappan, J. Dawson, and S. Lawrie, "The design of radar corner reflectors for the Australian geophysical observing system: A single design suitable for InSAR deformation monitoring and SAR calibration at multiple microwave frequency bands," Geosci. Australia, Australia, QLD, Canberra, Rec. Tech. Rep. 2015/03, 2015.

[13] I. Bozsó, E. Szűcs, L. Bányai, and V. Wesztergom, "Benchmark of C-band radar corner reflectors based on Sentinel-1 SAR images. First results in the monitoring of the Dunaszekcső landslide (Hungary) using corner reflectors," in *Proc. EGUGA*, 2018, p. 714.

[14] M. Garthwaite, "On the design of radar corner reflectors for deformation monitoring in multi-frequency InSAR," *Remote Sens.*, vol. 9, no. 7, p. 648, Jun. 2017.

[15] J. C. Curlander and R. N. McDonough, *Synthetic Aperture Radar: Systems and Signal Processing*. New York, NY, USA: Wiley, 1991.

[16] M. C. Garthwaite, S. Lawrie, J. Dawson, and M. Thankappan, "Corner reflectors as the tie between InSAR and GNSS measurements: Case study of resource extraction in Australia," in *Proc. FRINGE*, vol. 731, 2015, pp. 1–5.

[17] P. Dheenathayalan, M. C. Cuenca, P. Hoogeboom, and R. F. Hanssen, "Small reflectors for ground motion monitoring with InSAR," *IEEE Trans. Geosci. Remote Sens.*, vol. 55, no. 12, pp. 6703–6712, Dec. 2017.

[18] R. Bamler and M. Eineder, "Accuracy of differential shift estimation by correlation and split-bandwidth interferometry for wideband and delta-K SAR systems," *IEEE Geosci. Remote Sens. Lett.*, vol. 2, no. 2, pp. 151–155, Apr. 2005.

[19] R. Czikhardt, H. van der Marel, F. J. van Leijen, and R. F. Hanssen, "Estimating signal-to-clutter ratio of InSAR corner reflectors from SAR time series," *IEEE Geosci. Remote Sens. Lett.*, vol. 19, pp. 1–5, 2022.

[20] V. G. Ketelaar, *Satellite Radar Interferometry: Subsidence Monitoring Techniques*, vol. 14. Springer, 2009.

[21] G. Ketelaar, P. Marinkovic, and R. Hanssen, "Validation of point scatterer phase statistics in multi-pass InSAR," in *Proc. ENVISAT & ERS Symp.*, vol. 572, 2005.

[22] N. Adam, B. Kampes, and M. Eineder, "Development of a scientific permanent scatterer system: Modifications for mixed ERS/ENVISAT time series," in *Proc. ENVISAT & ERS Symp.*, vol. 572, 2005.

[23] S. Selvakumaran *et al.*, "Combined InSAR and terrestrial structural monitoring of bridges," *IEEE Trans. Geosci. Remote Sens.*, vol. 58, no. 10, pp. 7141–7153, Oct. 2020.

[24] D. Di Martire, A. Iodice, M. Ramondini, G. Ruello, and D. Calcaterra, "Combined observations of surface displacements using differential interferometry SAR (DInSAR) and traditional monitoring techniques," in *Proc. 8th Intern. Symp. Field Meas. Geomech.*, Berlin, Germany, 2011.

[25] I. Bozsó, L. Banyai, A. Hooper, E. Szucs, and V. Wesztergom, "Integration of Sentinel-1 interferometry and GNSS networks for derivation of 3-D surface changes," *IEEE Geosci. Remote Sens. Lett.*, vol. 18, no. 4, pp. 692–696, Apr. 2021.

[26] C. Li *et al.*, "Comprehensive calibration and validation site for information remote sensing," *Int. Arch. Photogramm., Remote Sens. Spatial Inf. Sci.*, vol. 40, no. 7, p. 1233, 2015.

[27] M. Del Soldato *et al.*, "Multisource data integration to investigate one century of evolution for the Agnone landslide (Molise, southern Italy)," *Landslides*, vol. 15, no. 11, pp. 2113–2128, 2018.

[28] M. C. Garthwaite, M. Hazelwood, S. Nancarrow, A. Hislop, and J. H. Dawson, "A regional geodetic network to monitor ground surface response to resource extraction in the northern surat basin, Queensland," *Austral. J. Earth Sci.*, vol. 62, no. 4, pp. 469–477, May 2015.

[29] C. Werner, U. Wegmüller, T. Strozzi, and A. Wiesmann, "Gamma SAR and interferometric processing software," in *Proc. ERS-ENVISAT Symp.*, Gothenburg, Sweden, vol. 1620, 2000, p. 1620.

[30] M. Lazecký *et al.*, "LiCSAR: An automatic InSAR tool for measuring and monitoring tectonic and volcanic activity," *Remote Sens.*, vol. 12, no. 15, p. 2430, Jul. 2020.

[31] A. W. Doerry and B. C. Brock, "Radar cross section of triangular trihedral reflector with extended bottom plate," Sandia Nat. Laboratories, Albuquerque, NM, USA, Sandia Rep., 2009.

[32] Y. Qin, D. Perissin, and L. Lei, "The design and experiments on corner reflectors for urban ground deformation monitoring in Hong Kong," *Int. J. Antennas Propag.*, vol. 2013, pp. 1–8, 2013.

[33] A. Chulliat *et al.*, "Out-of-cycle update of the US/UK world magnetic model for 2015–2020," Nat. Centers Environ. Inf., NOAA, 2019.

[34] J. J. Sousa, A. J. Hooper, R. F. Hanssen, and L. C. Bastos, "Comparative study of two different PS-InSAR approaches: DePSI vs. StaMPS," in *Proc. ESA Fringe Workshop*, 2009, pp. 1–8.

[35] A. Ferretti, C. Monti-Guarnieri, C. Rrati, and F. Rossa "InSAR principles: Guidelines for SAR interferometry processing and interpretation," ESA Publication, 2007.

[36] T. A. Herring, R. W. King, and S. M. McClusky, "Introduction to gamit/globk release 10.6," Massachusetts Inst. Technol., Cambridge, MA, USA, Tech. Rep., 2015.

[37] A. Pepe and R. Lanari, "On the extension of the minimum cost flow algorithm for phase unwrapping of multitemporal differential SAR interferograms," *IEEE Trans. Geosci. Remote Sens.*, vol. 44, no. 9, pp. 2374–2383, Sep. 2006.

[38] H.-J. Li, Y.-W. Kiang, and W. Chen, "Radar and inverse scattering," in *The Electrical Engineering Handbook*. Academic, 2005, pp. 671–690.

Krisztina Kelevitz received the Ph.D. degree in geophysics from ETH Zürich, Zürich, Switzerland, in 2017, for her research in using GNSS data in rapid earthquake moment tensor characterization.

She worked as a Post-Doctoral Researcher with the University of Colorado, Boulder, CO, USA, from 2017 to 2019, working on setting up an early warning system for the Yellowstone volcanic area using remote sensing InSAR data. She then became a Centre for the Observation and Modelling of Earthquakes, Volcanoes and Tectonics (COMET) Research Fellow at the University of Leeds, Leeds, U.K., where she continued to work on InSAR data applications, including natural hazard monitoring in the U.K. and a design and experiments of a novel corner reflector array for infrastructure monitoring.

Tim J Wright is a Professor of satellite geodesy with the University of Leeds, Leeds, U.K., the Director of COMET, Leeds, the NERC Centre for the Observation and Modelling of Earthquakes, Volcanoes and Tectonics, and the Co-Founder and the Director of SATSENSE Ltd. His work has been at the forefront of developing the use of satellite radar interferometry (InSAR) for measuring tectonic and volcanic deformation. Major achievements include the first demonstration that interseismic strain can be measured using InSAR, in this case for the North Anatolian Fault; the investigation of a series of major earthquakes using geodesy, seismology, and geomorphology, including Bam (Iran, 2003), Denali (Alaska, 2002), and Izmit (Turkey, 1999); mapping and modeling of precursory inflation at a volcanic center (Dabbahu, Ethiopia), and the subsequent discovery of a major rifting episode in Afar, Ethiopia. He has published more than 120 articles in major international journals, and his work is highly cited. He led the NERC-funded Afar Rift Consortium, a £3M project that is using a wide range of geophysical, geochemical, and geologic techniques to investigate how the crust grows at divergent plate boundaries, and co-led LICS, an NERC large grant to "Look Inside the Continents from Space," which is producing open-access InSAR data over global volcanic and tectonic areas from Sentinel-1.

Dr. Wright received the William Smith Fund of the Geological Society, in 2006, the Philip Leverhulme Prize, in 2014, the American Geoscience Union (AGU) Geodesy Section Award, he was the British Geophysical Association's Bullerwell Lecturer in 2015, and the Rosenstiel Award from the University of Miami. He was the Royal Astronomical Society's 2017 Harold Jeffreys Lecturer.

Andrew J Hooper (Senior Member, IEEE) received the M.S. and Ph.D. degrees in geophysics from Stanford University, Stanford, CA, USA, in 2002 and 2006, respectively, for his development of SAR persistent scatterer interferometry algorithms for geophysical applications.

From 2002 to 2003, he worked with the German Space Center (DLR) on algorithms for the TerraSAR-X satellite. Since 2006, he has been with the University of Iceland, Reykjavik, Iceland, before moving to the Delft University of Technology, Delft, Netherlands, in 2008. Since 2013, he has been a Professor of geophysics and geodesy with the University of Leeds, Leeds, U.K. His research interests include measuring and modeling deformation due to volcanic and tectonic processes and application of machine learning techniques to deformation data.

Dr. Hooper received the James B. Macelwane Medal by the American Geophysical Union, in 2016, given to outstanding early career scientists who have shown depth, breadth, impact, creativity, and novelty in their research, and is the Co-Founder and the Director of University spin-out SatSense, Leeds.

Sivasakthy Selvakumaran (Member, IEEE) received the B.A. and M.Eng. degrees in engineering and the Ph.D. degree in applied remote sensing from the Engineering Department, University of Cambridge, Cambridge, U.K., in 2010 and 2019, respectively, and the C.Eng. degree with MICE professional engineering chartership qualifications from the Institution of Civil Engineers (ICE), London, U.K., in 2015.

She worked in design, construction, and research and development roles within industry in Spain, Peru, and U.K. Her roles in industry included designing new structures on mega-projects like the Crossrail trainline in London, assessment to upgrade U.K. infrastructure assets, and working on sites to reconstruct housing destroyed by earthquakes. She has also worked in industry research and development roles for developing new solutions and technologies to change the way infrastructure is designed, constructed, and maintained. She spent part of her doctoral training as a Visiting Researcher with the German Aerospace Center (DLR), Oberpfaffenhofen, Germany, in 2019. She is the Isaac Newton Trust Fellow of engineering with the University of Cambridge. Her research interests include integration of remote sensing with structural monitoring to contribute toward sustainable and resilient cities.